In-situ reconstruction of $Bi_{60}In_2O_{93}$ nanotube for stable electroreduction of CO_2 at ampere-current densities

Zhipeng Chen [a,*,1], Dongdong Zhang [a,1], Quanzhu Li [a], Hongna Zhang [a], Yusi Zhao [a], Qingping Ke [a], Yan Yan [a], Licheng Liu [b], Mingkai Liu [a,*], Xiaojun He [a,*]

[a] School of Chemistry and Chemical Engineering, Anhui University of Technology, Ma'anshan 243032, China
[b] College of Chemistry & Chemical Engineering, Ocean University of China, Qingdao 266100, China

ARTICLE INFO

ABSTRACT

We report a unique Bi-In nanotube catalyst ($Bi_{60}In_2$ NT), which was prepared by in-situ reconstruction of a novel precursor of $Bi_{60}In_2O_{93}$. By virtue of the structural characteristics of hollow nanotubes and the modulated electronic structure by indium atom doping, $Bi_{60}In_2$ NT delivers an impressive partial current density of 1.03 A cm^{-2} with a high Faradaic efficiency (FE) of 95.3% for formate production. Moreover, $Bi_{60}In_2$ NT demonstrates a long-term stability of 48 h at a high current density of 1 A cm^{-2} in MEA cells. In-situ ATR-SEIRAS spectra confirm that doping of indium atoms enhances the adsorption strength of Bi sites to the *OCHO intermediate. Additionally, DFT calculations reveal that the charge redistribution between bismuth and indium atoms promotes the adsorption of *CO_2 intermediates and accelerates the charge transfer kinetics, which undoubtedly contributes to the enhanced activity.

1. Introduction

Using renewable electricity to catalyze CO_2 reduction to C_1-C_4 hydrocarbons is considered a promising route to implement the artificial carbon cycle [1,2]. Among the many products of CO_2 electrolysis, formic acid is the most value-added chemical feedstock due to its highest economic value (0.43 $ per k Wh^{-1}) produced at the per kilowatt-hour of electrical energy input [3,4]. However, the high thermodynamic stability of CO_2 molecule leads to the sluggish reaction kinetic, it is critical to develop highly active catalysts to improve the reaction efficiency [5]. Over the past few decades, a large number of catalysts have been explored to enhance the activity of CO_2 electroreduction reaction (CO_2RR), typical representatives are single-atom catalysts [5–9], Cu-based catalysts [10–14], molecular catalysts [15–17], and MOF/COF-based catalysts [18,19].

For the electroreduction of CO_2 to formic acid/formate, p-block metal catalysts, such as indium, tin, lead, and bismuth, etc. [4,20], especially bismuth-based catalysts are the most promising catalysts. Numerous research methods, such as size/dimensionality control [21–27], surface modification [28–31], defects/grain boundaries construction [32–35], doping engineering [36,37], etc., have been focused

on improving the intrinsic activity of bismuth-based catalysts, which promotes the Faradaic efficiency close to 100% for formate production. Furthermore, to overcome the mass transfer limitation caused by the low solubility of CO_2 in the electrolyte, novel electrolyzers such as flow cells/membrane electrode assembly cells that can create a gas-liquid-solid three-phase reaction interface have been developed to increase the current density to hundreds of milliamperes. Although the Faradaic efficiencies of producing formic acid/formate over bismuth-based catalysts are generally over 90% at current densities of several hundred milliamps [31,38,39], it remains challenge to electroreduction of CO_2 to formic acid/formate at ampere-level current densities with high stability [40].

Previous studies have revealed that the OCHO* is a key intermediate for the electroreduction of CO_2 to formic acid/formate, and a highly active catalyst should have moderate adsorption strength for OCHO* intermediates [41,42]. However, the low electronic density states of Bi 6p orbital near the Fermi level leads to the weak adsorption strength of bismuth-based catalysts for OCHO* intermediates [43]. Therefore, it is expected to further improve the activity by regulating the electronic structure of bismuth-based catalysts to optimize the adsorption strength of OCHO* intermediates [44]. Introducing heteroatom doping or

* Corresponding authors.
  E-mail addresses: chenzp@ahut.edu.cn (Z. Chen), liumingkai@ahut.edu.cn (M. Liu), xjhe@ahut.edu.cn (X. He).
1 These authors contributed equally.

constructing bimetallic interfaces is one of the effective ways to regulate the catalyst electronic structure [45–50]. In accordance with this understanding, the electron-rich indium atoms are introduced to regulate the electronic structure of bismuth nanotubes to enhance the adsorption strength of reaction intermediates in this study. On the other hand, constructing a hollow nanotube structure is conducive to improving the mass transfer efficiency in the CO_2RR process [32,37,51–54], thereby further enhancing the current density for formic acid/formate production.

Inspired by the above two aspects, we synthesized a novel precursor of $Bi_{60}In_2O_{93}$ by a "coaxial electrospinning-sacrificial template" method, which can be in-situ restructured to a hollow-structured In-doped Bi nanotube ($Bi_{60}In_2$ NT) under CO_2RR conditions. By virtue of the hollow nanotube structure and the regulation of the catalyst electronic structure by indium atom doping, the as-prepared catalyst delivers an ampere-level current density for of CO_2 reduction to formate with high stability. Besides, we combined in-situ ATR-SEIRAS spectra and DFT calculations to gain insight into the catalytic reaction mechanism.

2. Experimental section

2.1. Synthesis of $Bi_{60}In_{23}$ NT

$Bi_{60}In_{23}$ NT was synthesized by a three-step method of "coaxial electrospinning-pyrolysis-electroreduction reconstruction". Firstly, 0.045 g of $In(NO_3)_3$ and 0.655 g of $Bi(NO_3)_3 \cdot 5 H_2O$ were added to 8 mL of N, N-dimethylformamide (DMF) to prepare the outer layer solution for coaxial electrospinning. Simultaneously, 0.8 g of Poly-vinylpyrrolidone (PVP, $M_w = 1,300,000$) was add into 5 mL of DMF to prepare the inner layer solution for coaxial electrospinning. Then both solutions were stirred at room temperature overnight to prepare homogenous mixtures for the coaxial electrospinning. For the coaxial electrospinning process, the inner layer and outer layer solutions were injected into the compound nozzle via the liquid supply system, and the extruded spinning solution was subjected to a high voltage electric field to form a Taylor cone, which eventually formed $In(NO_3)_3/Bi(NO_3)_3/$ PAN@PVP composite fibers on the collector. In this study, the extrusion speed of the inner layer and outer layer solutions were respectively controlled at 0.2 and 0.5 mL h^{-1}. The distance between the needle and the collector was controlled at 15 cm and the high voltage was controlled at 18 kV. After the coaxial electrospinning steps, the prepared composite fibers were pre-oxidized at 220 °C for 1 h and pyrolyzed at 450 °C for 3 h in air. The PVP template in the inner layer of the composite fibers was volatilized during the pyrolysis process, resulting in the formation of a precursor of $Bi_{60}In_2O_{93}$ NT with a hollow nanotube structure. Finally, the precursor was loaded on a carbon paper and electroreduced at a controlled potential of − 0.8 V (vs. RHE) for 1 h to reconstruct into In doped Bi nanotube ($Bi_{60}In_2$ NT). BiIn NT catalysts with different In atom contents were prepared by adding different In $(NO_3)_3$ in the coaxial electrospinning process.

2.2. Synthesis of Bi NT

The synthesis steps of Bi NT are similar to those of $Bi_{60}In_2$ NT, except that $In(NO_3)_3$ is not added to the outer layer solution in coaxial electrospinning process. Briefly, the $Bi(NO_3)_3/$PAN@PVP composite fibers were firstly synthesized by the coaxial electrospinning method. Subsequently, the prepared composite fibers were pre-oxidized and pyrolyzed to synthesis Bi_2O_3 nanotubes (Bi_2O_3 NT). Finally, Bi_2O_3 NT was electrochemically reduced and reconstructed to prepare catalysts Bi nanotube (Bi NT).

3. Results and discussion

3.1. Synthesis and characterization

As illustrated in Fig. 1a, $In(NO_3)_3/Bi(NO_3)_3/$PAN@PVP composite fibers with coaxial cable structure were firstly prepared by an coaxial electrospinning method. Then the composite fibers were pyrolyzed in air to sacrifice the PVP template and form the hollow structured $Bi_{60}In_2O_{93}$ nanotube ($Bi_{60}In_2O_{93}$ NT). Finally, the $Bi_{60}In_2O_{93}$ NT was in situ reconstructed under electrochemical reduction conditions to prepare $Bi_{60}In_2$ NT. As a comparison, Bi NT (Bi nanotube) was prepared by the similar procedures as $Bi_{60}In_2O_{93}$ NT without adding $In(NO_3)_3$ during the coaxial electrospinning steps.

SEM images reveal that the precursor catalyst is a hollow tubular structure composed of nanoparticles with a size of ∼15 nm (Fig. 1b and c). TEM images confirm the formation of hollow structure (Fig. 1d and f), which is attributed to the volatilization of PVP fiber template formed in the inner layer of coaxial electrospinning. As indicated by XRD patterns (Fig. 2a), the precursor catalyst is composed of a special compound $Bi_{60}In_2O_{93}$. The ordered lattice fringes of 0.32 nm are assigned to the (201) plane of $Bi_{60}In_2O_{93}$ (Fig. 1e), agreeing well with the XRD results. If $In(NO_3)_3$ is not added during electrospinning, Bi_2O_3 nanotubes (Bi_2O_3 NT) are formed after pyrolysis (Fig. 2a and Fig. S1). The survey XPS spectrum demonstrates that $Bi_{60}In_2O_{93}$ NT contained only Bi, O and In elements (Fig. S2), which is also evidenced by the elemental mappings of TEM (Fig. 1g-i). The Bi 4 f peaks at 158.7 eV and 164.0 eV suggest a single oxidation state of Bi^{3+} of $Bi_{60}In_2O_{93}$ NT (Fig. 2b) [55].

Under the conditions of CO_2RR, the as-prepared $Bi_{60}In_2O_{93}$ NT is electrochemically reduced and reconstructed into In doped Bi nanotube ($Bi_{60}In_2$ NT). As shown in Fig. S3, the hollow nanotube structure is preserved after reconstruction. Only the XRD diffraction peaks of metallic Bi are observed, which can be attributed to the lower content of In atoms (provided by ICP-OES is 3.47 at%) and the doping of In atoms into the Bi crystal lattice. A slight shift towards higher diffraction angles is observed compared to the standard Bi crystal (PDF#44–1246) (Fig. 2c), which is attributed to the change in the crystal structure caused by the substitution of some larger Bi atoms by doping smaller In atoms. The Bi 4 f peaks at 158.7 eV and 164.0 eV indicate a metallic state of Bi^0 of $Bi_{60}In_2$ NT, coinciding well with the XRD analysis. Furthermore, the partial charge transfer of Bi atoms to adjacent In atoms of $Bi_{60}In_2$ NT is confirmed by the positive shift of Bi 4 f peaks compared with Bi NT (Fig. 2d). Additionally, the In 3d peaks at 451.4 eV and 443.8 eV suggest a metallic state of In^0 of $Bi_{60}In_2$ NT (Fig. S4).

3.2. CO_2 electroreduction performance evaluation

The activity of CO_2 electrolysis was evaluated in a gas-fed flow electrolyzer (Fig. 3a) [48,56]. LSV curves were recorded in CO_2-fed cells. As illustrated in Fig. S5, $Bi_{60}In_2$ NT shows larger current densities than Bi NT in CO_2-fed flow cells, indicating that $Bi_{60}In_2$ NT is more prone to catalyze the CO_2 electroreduction reaction. In order to more accurately evaluate the activity of CO_2RR, the electrolysis experiment was carried out by a controlled potential method. By virtue of the hollow nanotube structure, more active sites are exposed and mass transfer is facilitated, thus the total current densities (j_{total}) of both catalysts are much higher than that of typical bismuth-based catalysts (Fig. S6 and Table S1). Similar to the LSV curves, the j_{total} of $Bi_{60}In_2$ NT is conspicuously higher than that of Bi NT (Fig. S6). At a potential of − 1.3 V vs. RHE, the j_{total} of $Bi_{60}In_2$ NT exceeds 1.12 A cm^{-2}. Gas and liquid products were quantitatively analyzed by online GC and HPLC respectively during electrolysis. Only H_2, CO and formate were detected for CO_2RR (Figs. S7 and S8). As shown in Fig. 3b, $Bi_{60}In_2$ NT not only exhibits higher formate FEs than Bi NT, but also delivers formate FEs of over 90% in a wide potential range from − 0.9 to − 1.3 V. A highest formate FE of 95.3 ± 2.9% is observed for $Bi_{60}In_2$ NT at − 1.0 V. Consequently, $Bi_{60}In_2$ NT shows lower CO and H_2 FEs than Bi NT (Fig. S9). By virtue of
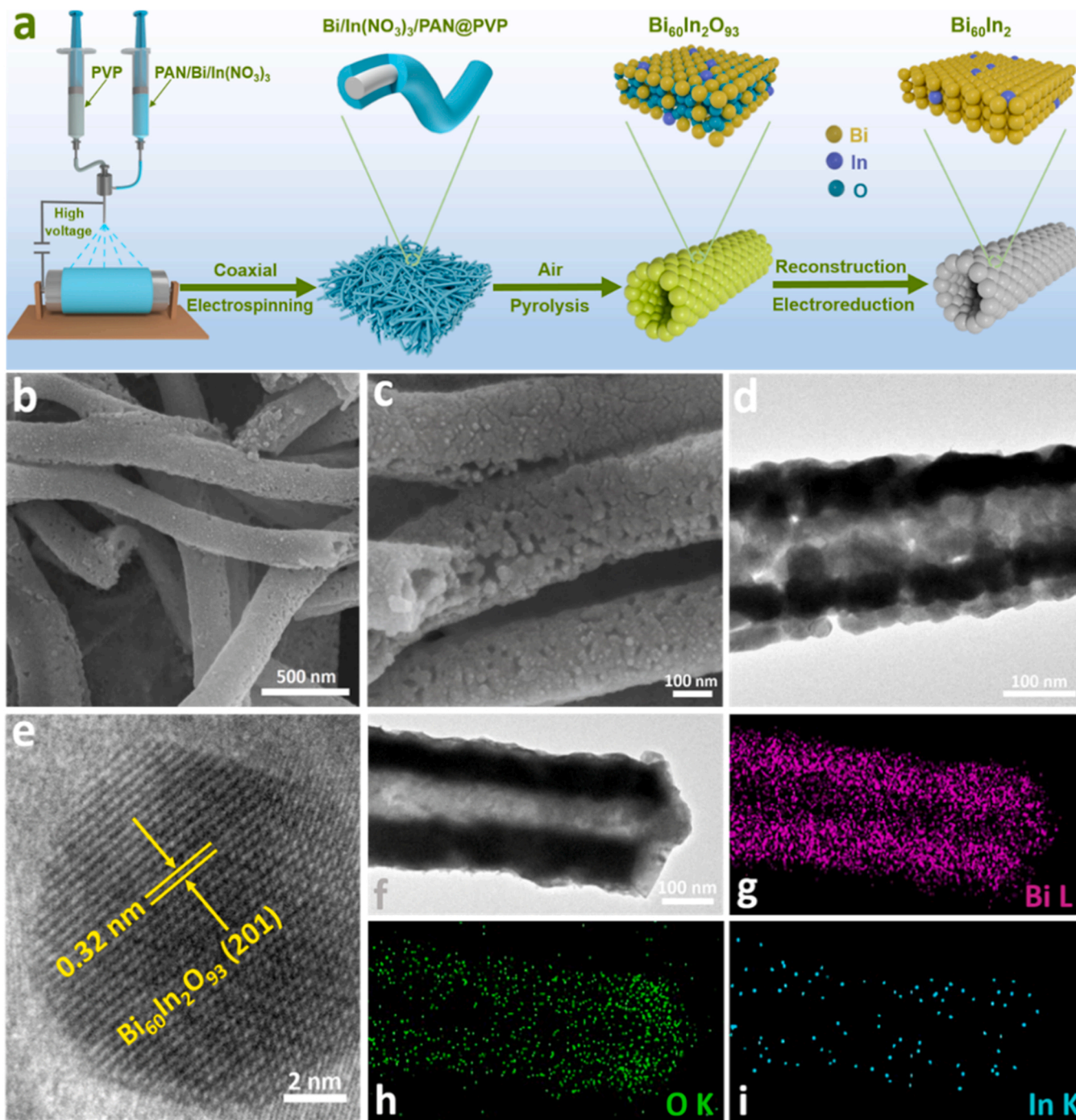
Fig. 1. (a) Schematic illustration of the preparation process for $Bi_{60}In_2$ NT. (b-c) SEM images, (d, f) TEM images, (e) HRTEM image and (g-i) elemental mappings of $Bi_{60}In_2O_{93}$ NT.

the large j_{total} and the wide operating potential range for high formate FEs, $Bi_{60}In_2$ NT demonstrates an impressive partial current density for formate production (j_{HCOO}^-) of 1.03 A cm^{-2} at -1.3 V, which is 1.52 times that of Bi NT (Fig. 3c). There is no doubt that $Bi_{60}In_2$ NT is a top-level catalyst for CO_2 electroreduction to formate (summarized in Table S1). Specifically, $Bi_{60}In_2$ nanorod ($Bi_{60}In_2$ NR) with non-hollow structure was also prepared to evaluate the effect of hollow structure on catalytic activity (Fig. S10a). It can be seen that the hollow structure significantly promotes the improvement of the current density and FEs of electroreduction of CO_2 to formate (Fig. S10b-d). In addition, the effect of In atom content on the catalytic activity was also evaluated. As presented in Fig. S11, the BiIn-3.5 NT (the content of In atoms is 3.5 at

%) shows higher formate FE and j_{HCOO}^- than other samples, indicating the that the optimum doping amount of In atom is about 3.5%.

The stability under industrially-relevant current densities is one of the important indicators of an ideal catalyst. Fig. 3d shows a long-term stability test of 500 min at a potential of -1.0 V. During long-term electrolysis, we used 2 L of catholyte for circulating flow to reduce the influence of pH change on the catalytic activity. It can be clearly seen that there is no significant attenuation in the reaction current density (from ~410 to ~390 mA cm^{-2}) in the long-term test. The fluctuation of current density is mainly caused by the pressure difference of gas and liquid on both sides of the GDEs. Meanwhile, the formate FEs can be kept above 89% in this electrolysis process. However, this flow cell cannot
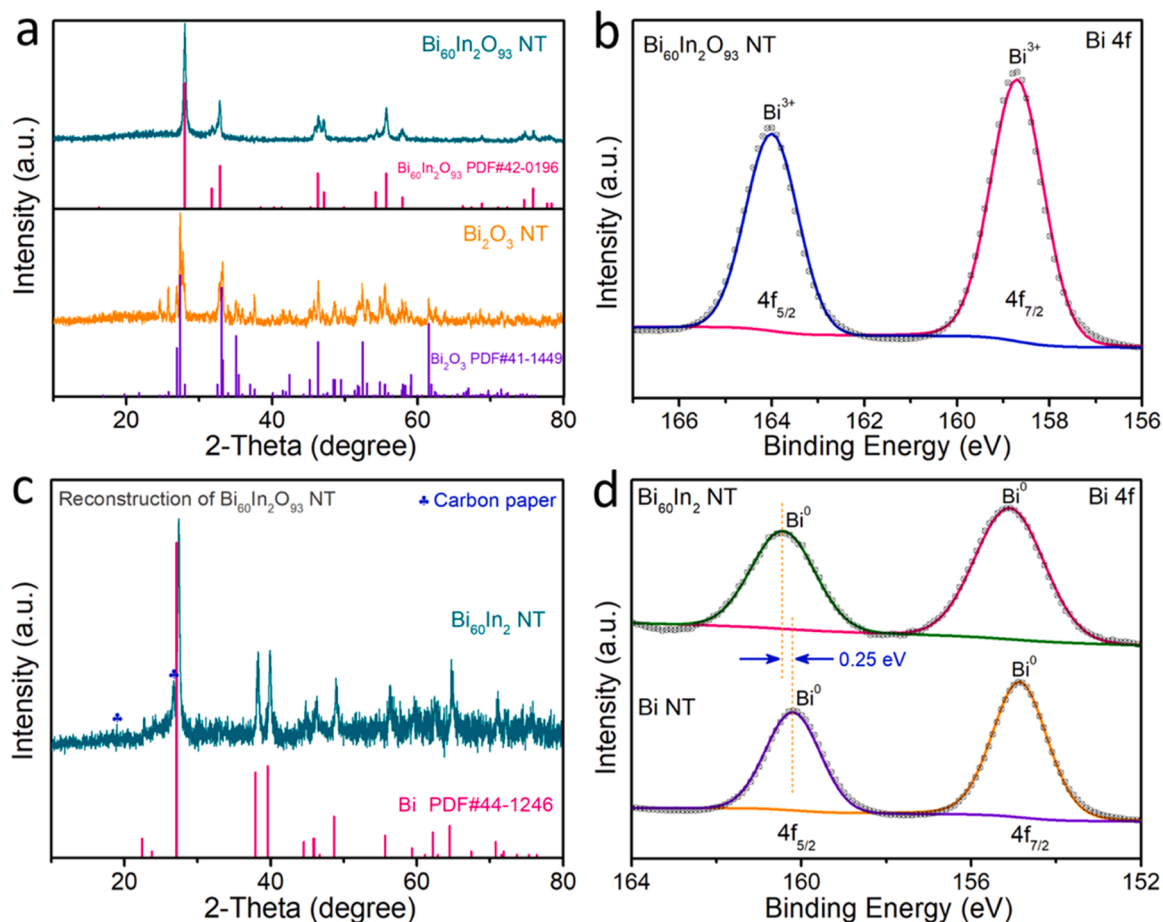
Fig. 2. (a) XRD patterns of Bi$_{60}$In$_2$O$_{93}$ NT and Bi$_2$O$_3$ NT. (b) Bi 4 f spectrum of Bi$_{60}$In$_2$O$_{93}$ NT. (c) XRD patterns of Bi$_{60}$In$_2$ NT (supported on carbon paper). (d) Bi 4 f spectra of Bi$_{60}$In$_2$ NT and Bi NT.
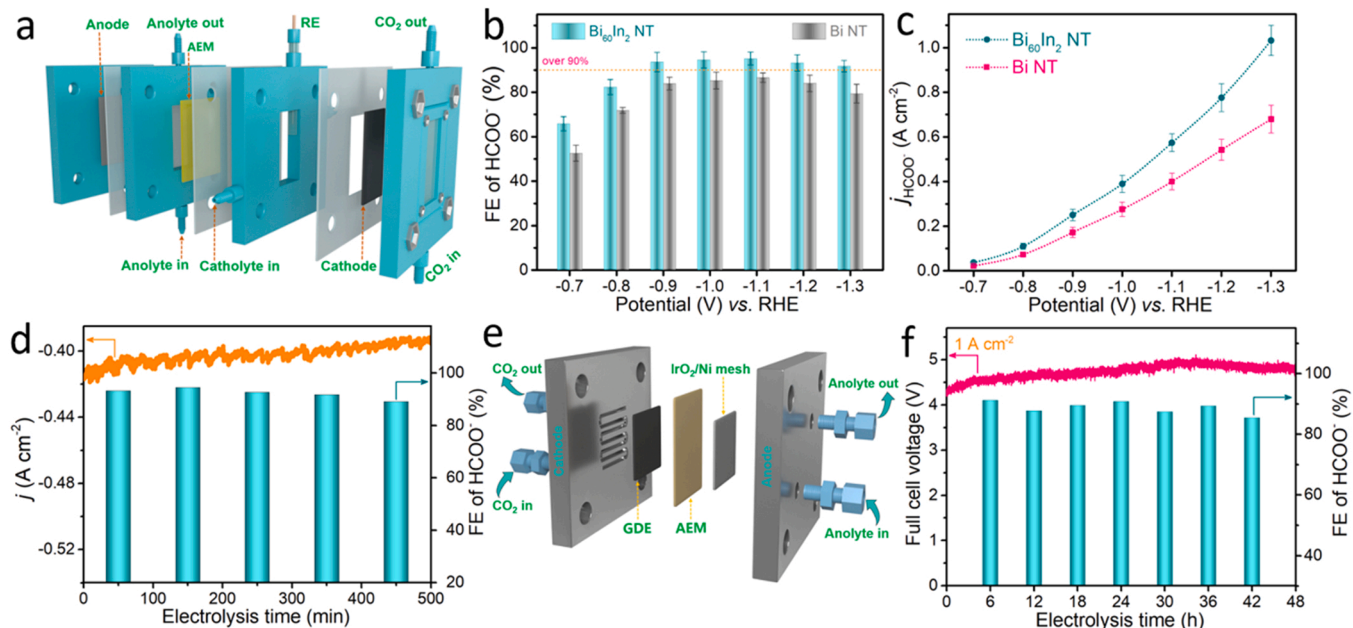
Fig. 3. (a) Schematic of the flow cell. (b) Formate FE and (c) j_{HCOO} of Bi$_{60}$In$_2$ NT and Bi NT. (d) Long-term stability electrolysis at − 1.0 V in flow cell. (e) Schematic of the MEA cell. (f) Long-term stability electrolysis at 1 A cm^{-2} in MEA cell.

keep the reaction stable for a longer time due to the GDEs being flooded, which caused by the precipitation of carbonate/bicarbonate on the GDEs surface in such a large current density and alkaline electrolyte. Therefore, a catholyte-free membrane electrode assembly (MEA) cell was used to improve the stability of the reaction. The physical photos and structural sketchs of the MEA cell are presented in Fig. S12 and Fig. 3e. As revealed by Fig. 3f, the electrolysis reaction can be carried out stably for more than 40 h at a large current density of 1 A cm^{-2}.

3.3. Reaction mchanism discussion

In-situ ATR-SEIRAS spectra were recorded under different applied potentials to investiagate the mechanism of CO_2 to formate. As presented in Fig. 4a and Fig. S13a, the peaks at ca. 1364 and 1645 cm^{-1} are ascribed to the adsorption of HCO_3^- [23,57,58]. Notably, the pronounced peak at ca. 1396 cm^{-1} appears at applied potentials more negative than -0.4 V (Fig. 4b), which can be assigned to the vibration of two oxygen bridge-bonded (O-C-O) formyloxyl radicals [59]. Additionally, the intensity of the peak gradually applied potentials become more negative, which is consistent with the trend of formate FEs changing with the applied potentials observed in the electrolysis experiments. Therefore, it can be inferred that *OCHO is the key intermediate for the formic acid/formate formation during CO_2RR. Moreover, the peak intensity for *OCHO of $Bi_{60}In_2$ NT is stronger than that of Bi NT (Fig. S13b), indicating the stronger adsorption strength to the *OCHO intermediate, which facilitates the further reduction of *OCHO intermediate to formate over $Bi_{60}In_2$ NT.

In order to compare the intrinsic activity of the two catalysts, the geometric j_{HCOO} (Fig. 4c) was normalized the ECSA (using C_{dl} instead of ECSA, Fig. S14) and catalyst loading. After normalization, the formate partial current density of $Bi_{60}In_2$ NT is conspicuously larger than that of Bi NT (Fig. 4c and Fig. S15), suggesting the higher intrinsic activity of $Bi_{60}In_2$ NT. As illustrated in Fig. S16, a smaller Tafel slope is observed for $Bi_{60}In_2$ NT than for Bi NT, indicating the faster reaction kinetics for $Bi_{60}In_2$ NT. Moreover, $Bi_{60}In_2$ NT delivers smaller R_s (bulk resistance) and R_{ct} (charge-transfer resistance) than that of Bi NT (Fig. 4d), which evidences that $Bi_{60}In_2$ NT has higher electronic conductivity and faster charge transfer kinetics. The above analysis results reveal that doping In atoms accelerates the kinetics of CO_2 electroreduction reaction.

DFT calculations were performed to further elucidate the origin of enhanced intrinsic activity. We constructed a simplified model of a four-layer Bi crystal (012) substituted with In atom to simulate the structure of $Bi_{60}In_2$ NT (Fig. S17). Referring to the previous results [60,61], there are two adsorption geometries of CO_2 on the catalyst surface: 1) the formation of *OCHO intermediate through the binding of oxygen atom to the catalyst, 2) the formation of *COOH intermediate through the binding of carbon atom to the catalyst, which may lead to distinct reaction pathways to form HCOOH and CO, respectively. First, the free energies for intermediates formation towards the two pathways were investigated. It can be seen that the formation of *OCHO is the rate-determining step in the reduction of CO_2 to HCOOH over the both two catalysts (Fig. 5a). Unequivocally, the energy barrier of *OCHO formation is.

lowered by In atom doping. Moreover, the free energy to produce *OCHO (0.66 and 0.95 eV) is lower than that to produce *COOH (1.12 eV) or *CO (1.24 eV) for the both two catalysts (Fig. 5a and b),
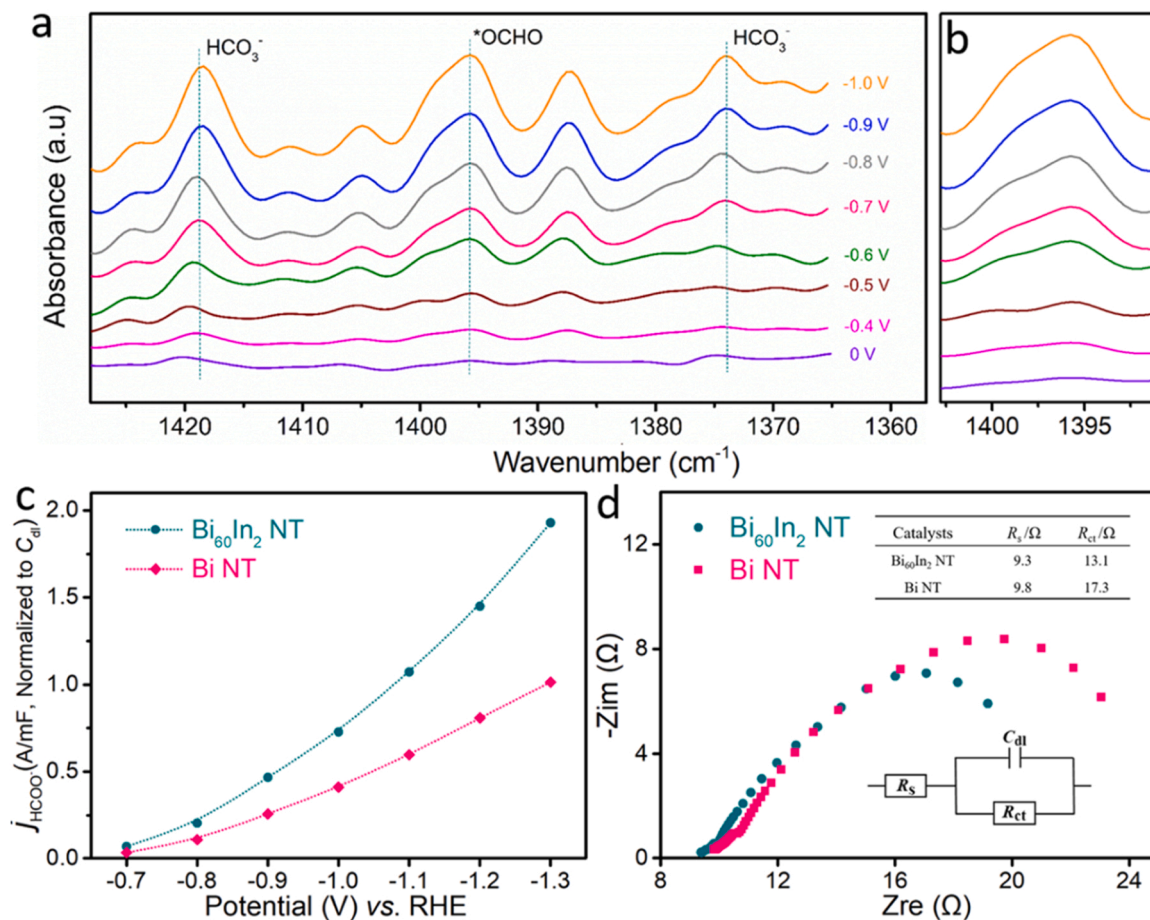
Fig. 4. (a) In situ ATR-SEIRAS characterization of $Bi_{60}In_2$ NT collected under different potentials. (b) The local enlarged plot of wavenumbers from 1403 to 1391 cm^{-1} in Fig. 4(a). (c) Formate partial current density normalized to the C_{dl} in flow cells. (d) Nyquist plot and the corresponding fitting equivalent circuit and numerical value of $Bi_{60}In_2$ NT and Bi NT.
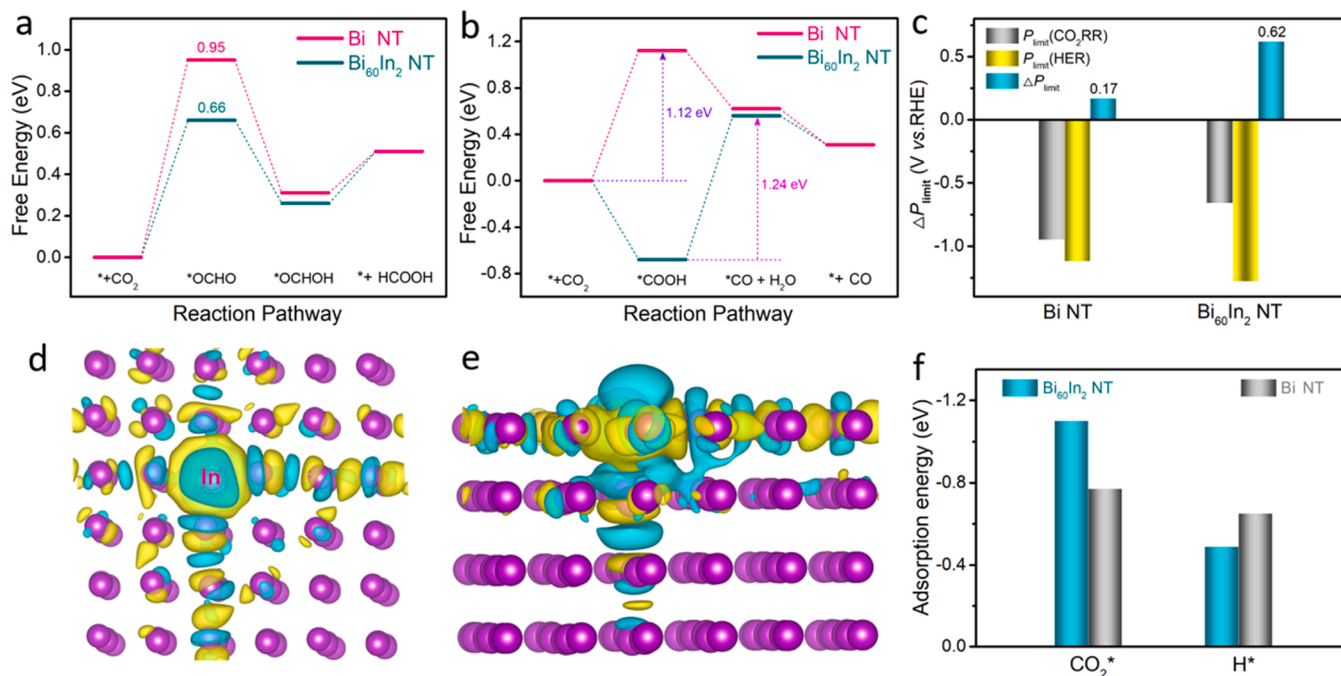
Fig. 5. Free energies of CO_2 reduction to HCOOH (a) and CO (b). (c) ΔP_{limit} of the CO_2RR and HER, $P_{limit} = -\Delta G/e$. (d) Top and (e) side view of charge density difference maps, yellow and cyan indicate the electrons accumulation of depletion, respectively. (f) Adsorption energies of CO* and H* .

indicating that the reduction of CO_2 to HCOOH is the energetically preferred pathway. We also calculated the free energies for the hydrogen evolution reaction (HER) (Fig. S18), and calculated the difference in the potentials of the rate-determining steps (ΔP_{limit}) for the CO_2RR and HER pathways. As presented in Fig. 5c, $Bi_{60}In_2$ NT exhibits a more positive ΔP_{limit} (0.62 V) than Bi NT (0.17 V), meaning a high formate selectivity of $Bi_{60}In_2$ NT, which well explains why $Bi_{60}In_2$ NT shows higher formate FEs than Bi NT in experiments. Then the mechanism of enhanced activity was further explored by investigating the difference in the electronic structure of catalysts and the adsorption energies of intermediates. The differential charge diagrams reveal that partial charge of Bi atoms transfers and accumulates on the surface of In atom (Fig. 5d and e), which coincides well with the XPS results (Fig. 2d). This charge redistribution is conducive to enhancing the adsorption of CO_2 on the catalysts surface. The calculation results of the adsorption energies show that $Bi_{60}In_2$ NT exhibits a stronger adsorption capacity for *CO_2 and a weaker adsorption capacity for protons (Fig. 5f), which facilitates CO_2RR and inhibits HER. Furthermore, the experimental results also evidence that $Bi_{60}In_2$ NT has a stronger adsorption capacity for CO_2(g) and *CO_2 than Bi NT (Figs. S19 and S20). Through the above analysis, we can draw a conclusion that the origin of the enhanced intrinsic activity is the redistribution of charge caused by In atoms doping, which promotes the adsorption of *CO_2 intermediates and accelerates the charge transfer kinetics.

4. Conclusion

In summary, a hollow-structured $Bi_{60}In_2$ nanotube catalyst was prepared by in-situ reconstruction of a novel precursor of $Bi_{60}In_2O_{93}$, which was prepared by "coaxial electrospinning-sacrificial template" method. The hollow tubular structure promotes the exposure of more active sites and the improvement of mass transfer efficiency, and moreover, the in-situ doping of In atoms induces the redistribution of the charge on Bi sites, which enhances the adsorption of *CO_2 intermediates and accelerates the charge transfer rates, thus promoting the electroreduction of CO_2 to formate at an impressive partial current density of 1.03 A cm^{-2} for formate production, outperforming the top-level

catalysts for the electroreduction of CO_2 to formate reported recently. In addition, the reaction mechanism was discussed in depth by in-situ ATR-SEIRAS spectra and DFT calculations.

CRediT authorship contribution statement

Zhipeng Chen: Conceptualization, Methodology, Validation, Investigation, Writing – original draft. **Dongdong Zhang:** Conceptualization, Methodology, Validation, Investigation, Writing – review & editing. **Quanzhu Li:** Methodology, Software, Formal analysis. **Hongna Zhang:** Methodology, Formal analysis, Investigation. **Yusi Zhao:** Validation, Formal anlaysis. **Qingping Ke:** Validation, Formal anlaysis. **Yan Yan**: Validation, Formal anlaysis. **Licheng Liu:** Validation, Formal anlaysis. **Mingkai Liu:** Conceptualization, Validation, Investigation, Writing – review & editing, Supervision. **Xiaojun He**: Conceptualization, Writing – review & editing, Supervision, Project administration.

Declaration of Competing Interest

The authors declare that they have no known competing financial interests or personal relationships that could have appeared to influence the work reported in this paper.

Data Availability

Data will be made available on request.

Acknowledgements

Appendix A. Supporting information

Supplementary data associated with this article can be found in the online version at doi:10.1016/j.apcatb.2023.123342.

References

[1] G. Wang, J. Chen, Y. Ding, P. Cai, L. Yi, Y. Li, C. Tu, Y. Hou, Z. Wen, L. Dai, Electrocatalysis for CO_2 conversion: from fundamentals to value-added products, Chem. Soc. Rev. 50 (2021) 4993–5061.

[2] S. Jin, Z. Hao, K. Zhang, Z. Yan, J. Chen, Advances and challenges for the electrochemical reduction of CO_2 to CO: from fundamentals to industrialization, Angew. Chem. Int. Ed. 60 (2021) 20627–20648.

[3] M.G. Kibria, J.P. Edwards, C.M. Gabardo, C.T. Dinh, A. Seifitokaldani, D. Sinton, E. H. Sargent, Electrochemical CO_2 reduction into chemical feedstocks: from mechanistic electrocatalysis models to system design, Adv. Mater. 31 (2019), 1807166.

[4] N. Han, P. Ding, L. He, Y. Li, Y. Li, Promises of main group metal-based nanostructured materials for electrochemical CO_2 reduction to formate, Adv. Energy Mater. 10 (2020), 1902338.

[5] L. Wang, W. Chen, D. Zhang, Y. Du, R. Amal, S. Qiao, J. Wu, Z. Yin, Surface strategies for catalytic CO_2 reduction: from two-dimensional materials to nanoclusters to single atoms, Chem. Soc. Rev. 48 (2019) 5310–5349.

[6] W. Zheng, F. Chen, Q. Zeng, Z. Li, B. Yang, L. Lei, Q. Zhang, F. He, X. Wu, Y. Hou, A universal principle to accurately synthesize atomically dispersed metal-N_4 sites for CO_2 electroreduction, Nano-Micro Lett. 12 (2020) 108.

[7] Y. Wang, Y. Liu, W. Liu, J. Wu, Q. Li, Q. Feng, Z. Chen, X. Xiong, D. Wang, Y. Lei, Regulating the coordination structure of metal single atoms for efficient electrocatalytic CO_2 reduction, Energy Environ. Sci. 13 (2020) 4609–4624.

[8] T.N. Nguyen, M. Salehi, Q.V. Le, A. Seifitokaldani, C.T. Dinh, Fundamentals of electrochemical CO_2 reduction on single-metal-atom catalysts, ACS Catal. 10 (2020) 10068–10095.

[9] C. Wang, X. Hu, X. Hu, X. Liu, Q. Guan, R. Hao, Y. Liu, W. Li, Typical Transition metal single-atom catalysts with a metal-pyridine N structure for efficient CO_2 electroreduction, Appl. Catal. B-Environ. 296 (2021), 120331.

[10] S. Nitopi, E. Bertheussen, S.B. Scott, X. Liu, A.K. Engstfeld, S. Horch, B. Seger, I. E. Stephens, K. Chan, C. Hahn, Progress and perspectives of electrochemical CO_2 reduction on copper in aqueous electrolyte, Chem. Rev. 119 (2019) 7610–7672.

[11] J. Yu, J. Wang, Y. Ma, J. Zhou, Y. Wang, P. Lu, J. Yin, R. Ye, Z. Zhu, Z. Fan, Recent progresses in electrochemical carbon dioxide reduction on copper-based catalysts toward multicarbon products, Adv. Funct. Mater. 31 (2021), 2102151.

[12] C. Xiao, J. Zhang, Architectural design for enhanced C_2 product selectivity in electrochemical CO_2 reduction using Cu-based catalysts: a review, ACS Nano 15 (2021) 7975–8000.

[13] J.C. Bui, C. Kim, A.J. King, O. Romiluyi, A. Kusoglu, A.Z. Weber, A.T. Bell, Engineering catalyst-electrolyte microenvironments to optimize the activity and selectivity for the electrochemical reduction of CO_2 on Cu and Ag, Acc. Chem. Res. 55 (2022) 484–494.

[14] S. Liu, B. Zhang, L. Zhang, J. Sun, Rational design strategies of Cu-based electrocatalysts for CO_2 electroreduction to C_2 products, J. Energy Chem. 71 (2022) 63–82.

[15] K. Elouarzaki, V. Kannan, V. Jose, H.S. Sabharwal, J.M. Lee, Recent trends, benchmarking, and challenges of electrochemical reduction of CO_2 by molecular catalysts, Adv. Energy Mater. 9 (2019), 1900090.

[16] Y. Wu, Z. Jiang, X. Lu, Y. Liang, H. Wang, Domino electroreduction of CO_2 to methanol on a molecular catalyst, Nature 575 (2019) 639–642.

[17] X. Zhang, Y. Wang, M. Gu, M. Wang, Z. Zhang, W. Pan, Z. Jiang, H. Zheng, M. Lucero, H. Wang, Molecular engineering of dispersed nickel phthalocyanines on carbon nanotubes for selective CO_2 reduction, Nat. Energy 5 (2020) 684–692.

[18] S.S.A. Shah, T. Najam, M. Wen, S.-Q. Zang, A. Waseem, H.-L. Jiang, Metal-organic framework-based electrocatalysts for CO_2 reduction, Small Struct. 3 (2022), 2100090.

[19] H. Zhong, M. Wang, G. Chen, R. Dong, X. Feng, Two-dimensional conjugated metal-organic frameworks for electrocatalysis: opportunities and challenges, ACS Nano 16 (2022) 1759–1780.

[20] H. Liu, Y. Su, Z. Liu, H. Chuai, S. Zhang, X. Ma, Tailoring microenvironment for enhanced electrochemical CO_2 reduction on ultrathin tin oxide derived nanosheets, Nano Energy 105 (2023), 108031.

[21] F. Yang, A.O. Elnabawy, R. Schimmenti, P. Song, J. Wang, Z. Peng, S. Yao, R. Deng, S. Song, Y. Lin, Bismuthene for highly efficient carbon dioxide electroreduction reaction, Nat. Commun. 11 (2020) 1088.

[22] L. Yi, J. Chen, P. Shao, J. Huang, X. Peng, J. Li, G. Wang, C. Zhang, Z. Wen, Molten-salt-assisted synthesis of bismuth nanosheets for long-term continuous electrocatalytic conversion of CO_2 to formate, Angew. Chem. Int. Ed. 59 (2020) 20112–20119.

[23] C. Cao, D.D. Ma, J.F. Gu, X. Xie, G. Zeng, X. Li, S.G. Han, Q.L. Zhu, X.T. Wu, Q. Xu, Metal-organic layers leading to atomically thin bismuthene for efficient carbon dioxide electroreduction to liquid fuel, Angew. Chem. Int. Ed. 59 (2020) 15014–15020.

[24] N. Han, Y. Wang, H. Yang, J. Deng, J. Wu, Y. Li, Y. Li, Ultrathin bismuth nanosheets from in situ topotactic transformation for selective electrocatalytic CO_2 reduction to formate, Nat. Commun. 9 (2018) 1320.

[25] X. Zhang, J. Fu, Y. Liu, X.-D. Zhou, J. Qiao, Bismuth anchored on MWCNTs with controlled ultrafine nanosize enables high-efficient electrochemical reduction of carbon dioxide to formate fuel, ACS Sustain. Chem. Eng. 8 (2020) 4871–4876.

[26] L. Lin, X. He, X.G. Zhang, W. Ma, B. Zhang, D. Wei, S. Xie, Q. Zhang, X. Yi, Y. Wang, A nanocomposite of bismuth clusters and $Bi_2O_2CO_3$ sheets for highly efficient electrocatalytic reduction of CO_2 to formate, Angew. Chem. Int. Ed. 62 (2023), e202214959.

[27] W. Ma, J. Bu, Z. Liu, C. Yan, Y. Yao, N. Chang, H. Zhang, T. Wang, J. Zhang, Monoclinic scheelite bismuth vanadate derived bismuthene nanosheets with rapid kinetics for electrochemically reducing carbon dioxide to formate, Adv. Funct. Mater. 31 (2021), 2006704.

[28] G. Wen, D.U. Lee, B. Ren, F.M. Hassan, G. Jiang, Z.P. Cano, J. Gostick, E. Croiset, Z. Bai, L. Yang, Orbital interactions in Bi-Sn bimetallic electrocatalysts for highly selective electrochemical CO_2 reduction toward formate production, Adv. Energy Mater. 8 (2018), 1802427.

[29] Z. Wu, H. Wu, W. Cai, Z. Wen, B. Jia, L. Wang, W. Jin, T. Ma, Engineering bismuth-tin interface in bimetallic aerogel with a 3D porous structure for highly selective electrocatalytic CO_2 reduction to HCOOH, Angew. Chem. Int. Ed. 60 (2021) 12554–12559.

[30] W. Zhang, S. Yang, M. Jiang, Y. Hu, C. Hu, X. Zhang, Z. Jin, Nanocapillarity and nanoconfinement effects of pipet-like bismuth@carbon nanotubes for highly efficient electrocatalytic CO_2 reduction, Nano Lett. 21 (2021) 2650–2657.

[31] P. Deng, F. Yang, Z. Wang, S. Chen, Y. Zhou, S. Zaman, B.Y. Xia, Metal-organic framework-derived carbon nanorods encapsulating bismuth oxides for rapid and selective CO_2 electroreduction to formate, Angew. Chem. Int. Ed. 59 (2020) 10807–10813.

[32] Q. Gong, P. Ding, M. Xu, X. Zhu, M. Wang, J. Deng, Q. Ma, N. Han, Y. Zhu, J. Lu, Structural defects on converted bismuth oxide nanotubes enable highly active electrocatalysis of carbon dioxide reduction, Nat. Commun. 10 (2019) 2807.

[33] L. Li, D.-K. Ma, F. Qi, W. Chen, S. Huang, Bi nanoparticles/Bi_2O_3 nanosheets with abundant grain boundaries for efficient electrocatalytic CO_2 reduction, Electrochim. Acta 298 (2019) 580–586.

[34] X. Fu, Ja Wang, X. Hu, K. He, Q. Tu, Q. Yue, Y. Kang, Scalable chemical interface confinement reduction BiOBr to bismuth porous nanosheets for electroreduction of carbon dioxide to liquid fuel, Adv. Funct. Mater. 32 (2022), 2107182.

[35] X. Zhang, X. Sun, S.-X. Guo, A.M. Bond, J. Zhang, Formation of lattice-dislocated bismuth nanowires on copper foam for enhanced electrocatalytic CO_2 reduction at low overpotential, Energy Environ. Sci. 12 (2019) 1334–1340.

[36] J.H. Zhou, K. Yuan, L. Zhou, Y. Guo, M.Y. Luo, X.Y. Guo, Q.Y. Meng, Y.W. Zhang, Boosting electrochemical reduction of CO_2 at a low overpotential by amorphous Ag-Bi-S-O decorated Bi^0 nanocrystals, Angew. Chem. Int. Ed. 58 (2019) 14197–14201.

[37] M. Wu, Y. Xiong, B. Hu, Z. Zhang, B. Wei, L. Li, J. Hao, W. Shi, Indium doped bismuth subcarbonate nanosheets for efficient electrochemical reduction of carbon dioxide to formate in a wide potential window, J. Colloid Interface Sci. 624 (2022) 261–269.

[38] F.P. García de Arquer, O.S. Bushuyev, P. De Luna, C.T. Dinh, A. Seifitokaldani, M. I. Saidaminov, C.S. Tan, L.N. Quan, A. Proppe, M.G. Kibria, 2D metal oxyhalide-derived catalysts for efficient CO_2 electroreduction, Adv. Mater. 30 (2018), 1802858.

[39] X. Yang, Q. Wang, F. Chen, H. Zang, C. Liu, N. Yu, B. Geng, In-situ electrochemical restructuring of Cu_2BiS_x solid solution into Bi/Cu_xS_y heterointerfaces enabling stabilization intermediates for high-performance CO_2 electroreduction to formate, Nano Res. 16 (2023) 7974–7981.

[40] D. Wang, K. Chang, Y. Zhang, Y. Wang, Q. Liu, Z. Wang, D. Ding, Y. Cui, C. Pan, Y. Lou, Y. Zhu, Y. Zhang, Unravelling the electrocatalytic activity of bismuth nanosheets towards carbon dioxide reduction: edge plane versus basal plane, Appl. Catal. B-Environ. 299 (2021), 120693.

[41] C. Qiu, K. Qian, J. Yu, M. Sun, S. Cao, J. Gao, R. Yu, L. Fang, Y. Yao, X. Lu, T. Li, B. Huang, S. Yang, MOF-transformed $In_2O_{3-x}@C$ nanocorn electrocatalyst for efficient CO_2 reduction to HCOOH, Nano-Micro Lett. 14 (2022) 167.

[42] Z. Chen, X. Zhang, M. Jiao, K. Mou, X. Zhang, L. Liu, Engineering electronic structure of stannous sulfide by amino-functionalized carbon: toward efficient electrocatalytic reduction of CO_2 to formate, Adv. Energy Mater. 10 (2020), 1903664.

[43] M. Zhao, Y. Gu, W. Gao, P. Cui, H. Tang, X. Wei, H. Zhu, G. Li, S. Yan, X. Zhang, Z. Zou, Atom vacancies induced electron-rich surface of ultrathin Bi nanosheet for efficient electrochemical CO_2 reduction, Appl. Catal. B-Environ. 266 (2020), 118625.

[44] T. Fan, W. Ma, M. Xie, H. Liu, J. Zhang, S. Yang, P. Huang, Y. Dong, Z. Chen, X. Yi, Achieving high current density for electrocatalytic reduction of CO_2 to formate on bismuth-based catalysts, Cell Rep. Phys. Sci. 2 (2021), 100353.

[45] J. Wang, S. Ning, M. Luo, D. Xiang, W. Chen, X. Kang, Z. Jiang, S. Chen, In-Sn alloy core-shell nanoparticles: In-doped SnO_x shell enables high stability and activity towards selective formate production from electrochemical reduction of CO_2, Appl. Catal. B-Environ. 288 (2021) 119979.

[46] D. Wu, R. Feng, C. Xu, P.-F. Sui, J. Zhang, X.-Z. Fu, J.-L. Luo, Regulating the Electron Localization of Metallic Bismuth for Boosting CO_2 Electroreduction, Nano-Micro Lett. 14 (2022) 38.

[47] Y. Guan, X. Zhang, Y. Zhang, T.N.V. Karsili, M. Fan, Y. Liu, B. Marchetti, X.-D. Zhou, Achieving high selectivity towards electro-conversion of CO_2 using In-doped Bi derived from metal-organic frameworks, J. Colloid Interface Sci. 612 (2022) 235–245.

[48] Z. Chen, G. Yu, B. Li, X. Zhang, M. Jiao, N. Wang, X. Zhang, L. Liu, In situ carbon encapsulation confined nickel-doped indium oxide nanocrystals for boosting CO_2 electroreduction to the industrial level, ACS Catal. 11 (2021) 14596–14604.

[49] Q. Wang, X. Yang, H. Zang, F. Chen, C. Wang, N. Yu, B. Geng, Metal-organic framework-derived BiIn bimetallic oxide nanoparticles embedded in carbon networks for efficient electrochemical reduction of CO_2 to formate, Inorg. Chem. 61 (2022) 12003–12011.

[50] Q. Wang, X. Yang, H. Zang, C. Liu, J. Wang, N. Yu, L. Kuai, Q. Qin, B. Geng, InBi bimetallic sites for efficient electrochemical reduction of CO_2 to HCOOH, Small (2023), 2303172.

[51] K. Fan, Y. Jia, Y. Ji, P. Kuang, B. Zhu, X. Liu, J. Yu, Curved surface boosts electrochemical CO_2 reduction to formate via bismuth nanotubes in a wide potential window, ACS Catal. 10 (2020) 358–364.

[52] Z. Chen, D. Zhang, Y. Zhao, D. Jia, H. Zhang, L. Liu, X. He, Indium oxide induced electron-deficient indium hollow nanotubes for stable electroreduction of CO_2 at industrial current densities, Chem. Eng. J. 464 (2023), 142573.

[53] S. Liu, X.F. Lu, J. Xiao, X. Wang, X.W. Lou, Bi_2O_3 nanosheets grown on multi-channel carbon matrix to catalyze efficient CO_2 electroreduction to HCOOH, Angew. Chem. Int. Ed. 58 (2019) 13828–13833.

[54] H. Rabiee, L. Ge, X. Zhang, S. Hu, M. Li, S. Smart, Z. Zhu, Z. Yuan, Shape-tuned electrodeposition of bismuth-based nanosheets on flow-through hollow fiber gas diffusion electrode for high-efficiency CO_2 reduction to formate, Appl. Catal. B-Environ. 286 (2021), 119945.

[55] C.W. Lee, J.S. Hong, K.D. Yang, K. Jin, J.H. Lee, H.-Y. Ahn, H. Seo, N.-E. Sung, K. T. Nam, Selective electrochemical production of formate from carbon dioxide with bismuth-based catalysts in an aqueous electrolyte, ACS Catal. 8 (2018) 931–937.

[56] Z. Chen, X. Zhang, W. Liu, M. Jiao, K. Mou, X. Zhang, L. Liu, Amination strategy to boost the CO_2 electroreduction current density of M-N/C single-atom catalysts to the industrial application level, Energy Environ. Sci. 14 (2021) 2349–2356.

[57] B. Wulan, X. Cao, D. Tan, J. Ma, J. Zhang, To stabilize oxygen on In/In_2O_3 heterostructure via joule heating for efficient electrocatalytic CO_2 reduction, Adv. Funct. Mater. 33 (2023), 2209114.

[58] Q. Zhang, M. Sun, C.-Y. Yuan, Q.-W. Sun, B. Huang, H. Dong, Y.-W. Zhang, Strong electronic coupling effects at the heterojunction interface of SnO_2 nanodots and g-C_3N_4 for enhanced CO_2 electroreduction, ACS Catal. 13 (2023) 7055–7066.

[59] Y. Li, J. Chen, S. Chen, X. Liao, T. Zhao, F. Cheng, H. Wang, In situ confined growth of bismuth nanoribbons with active and robust edge sites for boosted CO_2 electroreduction, ACS Energy Lett. 7 (2022) 1454–1461.

[60] J.S. Yoo, R. Christensen, T. Vegge, J.K. Norskov, F. Studt, Theoretical insight into the trends that guide the electrochemical reduction of carbon dioxide to formic acid, Chemsuschem 9 (2016) 358–363.

[61] C.W. Lee, N.H. Cho, K.D. Yang, K.T. Nam, Reaction mechanisms of the electrochemical conversion of carbon dioxide to formic acid on tin oxide electrodes, Chemelectrochem 4 (2017) 2130–2136.